Alwyn Scott

Neuroscience
A Mathematical Primer

With 58 Figures

Springer

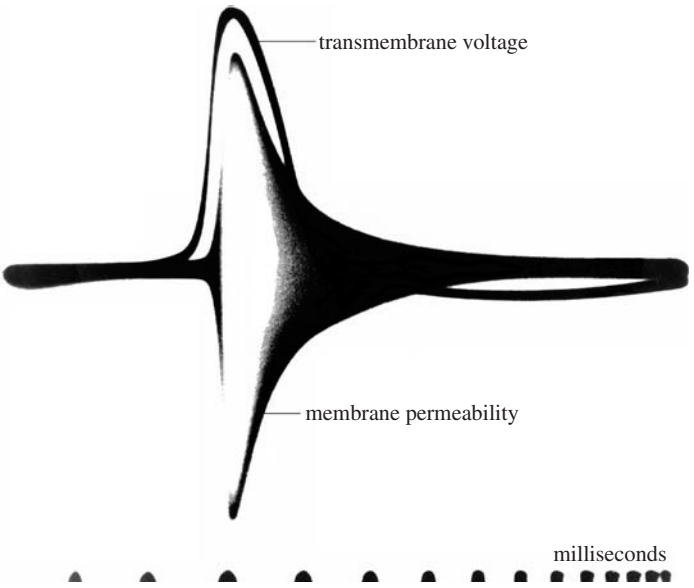

Figure 1.1. An early oscillogram of the change in membrane conductance (band) and membrane voltage (line) with time during the passage of a nerve impulse on a squid axon. (Time increases to the right, and the marks along the lower edge indicate intervals of 1 ms.) (Courtesy of K.S. Cole.)

a maximum value of about 100 millivolts (mV) in a fraction of a millisecond (ms), and this initial rise is called the *wave front* or *leading edge* of the nerve impulse. The impulse voltage then relaxes more slowly back to its resting level over a time interval of several milliseconds. The broad band also shown in the figure is a measure of changes of membrane permeability (or ionic conductance) from a resting value.[3]

Curiously overlooked by Western scientists was an important paper that also appeared in 1938 by the Soviet scientists Yakov Zeldovich and David Frank-Kamenetsky [71]. Addressing the problem of flame-front propagation, they proposed a simple *nonlinear partial differential equation* (PDE) for nonlinear diffusion in an active medium in which the independent variables were time and distance in the direction of propagation. In this paper, the authors solved their nonlinear PDE for an analytic solution describing a stable traveling wave: the flame front.

As we will see in Chapter 5, this simple equation also predicts both the speed of a nerve impulse on a squid axon and the shape of its leading edge. If these results had been noted by applied mathematicians and be-

[3]To measure ionic conductance, an ac bridge was balanced at the resting level of membrane permeability; thus, the width of the band indicates unbalance of the bridge, which stems from the change of permeability during the impulse.

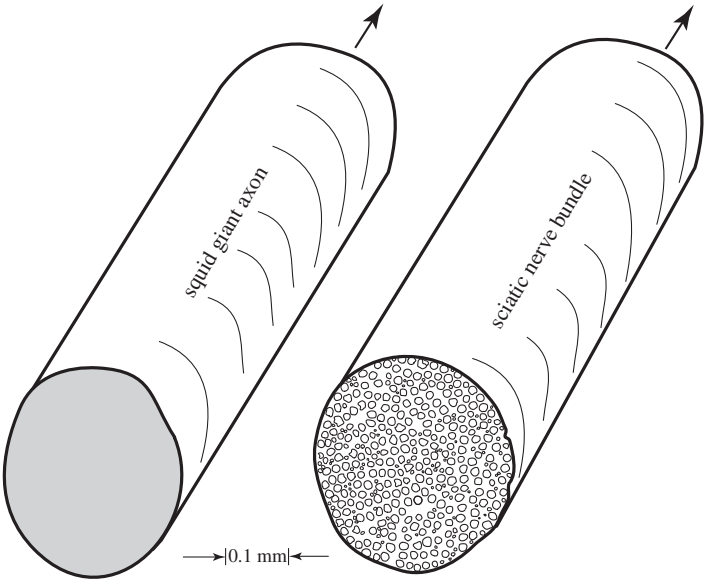

Figure 1.2. Comparison of the squid giant axon (left) and the sciatic nerve bundle controlling the leg muscle of a rabbit (right). There are about 375 myelinated fibers in the rabbit nerve, each conducting an individual train of nerve impulses at up to 80 m/s, about four times faster than the impulse velocity on a squid nerve. (Data from Young [70].)

the qualitative nature of nerve impulse propagation. Continuing throughout the 1970s, this tardy yet essential effort has deepened our understanding of several key phenomena, including all-or-nothing propagation, threshold conditions for nerve impulse formation, impulse stability, impulse response to variations in fiber geometry, decremental conduction, speed of periodic impulse trains, and effects of temperature and narcotization, all of which are considered in this book.

Presently, the propagation of a nerve impulse on a smooth fiber is a well-understood area of mathematical biology, the salient features of which should be appreciated by all serious students of neuroscience.

Interestingly, the sciatic nerve—first studied by Galvani in the late eighteenth century and used as a basic preparation for much subsequent neuroscience research—is not a smooth fiber; in fact, it is not even a single fiber. Like all vertebrate motor nerves, the sciatic nerve is a *bundle* of individual fibers, each carrying a different train of impulses from the spinal cord to a muscle, as was emphasized in a classic image prepared by J.Z. Young from which Figure 1.2 is drawn.

In this figure, we see a squid nerve compared with a rabbit sciatic nerve bundle on the same scale of distance showing that the rabbit nerve has about 375 information channels to one for the squid nerve. Because rabbit

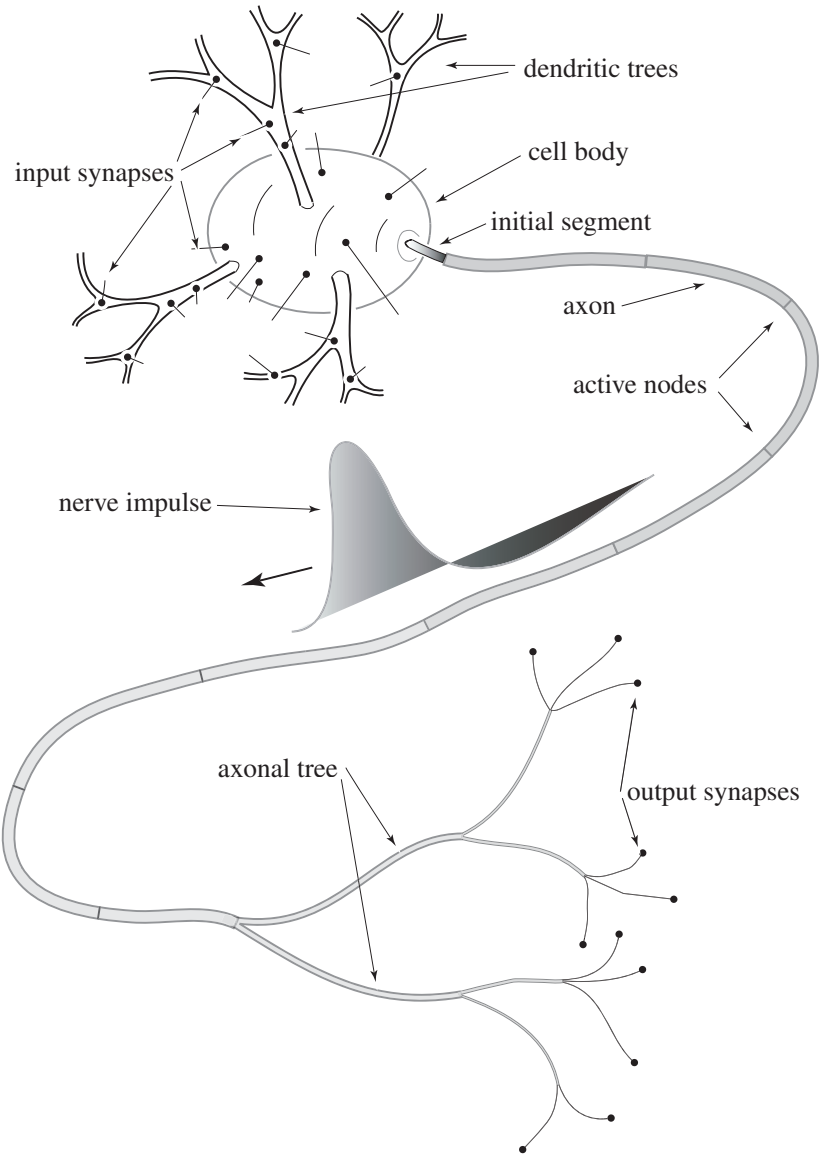

Figure 2.1. A cartoon of a typical nerve cell, or *neuron*, showing *dendrites* that gather incoming information from input *synapses* and an *axon* carrying outgoing signals through the branches of the axonal tree to other neurons or muscles.

- *Axons*: The *axon,* or outgoing channel of a neuron carries information away from the *cell body* and toward the output terminals. As indicated in Figure 1.2 of the previous chapter, an axon may be a relatively large fiber, such as the squid giant axon, or one of the many smaller fibers

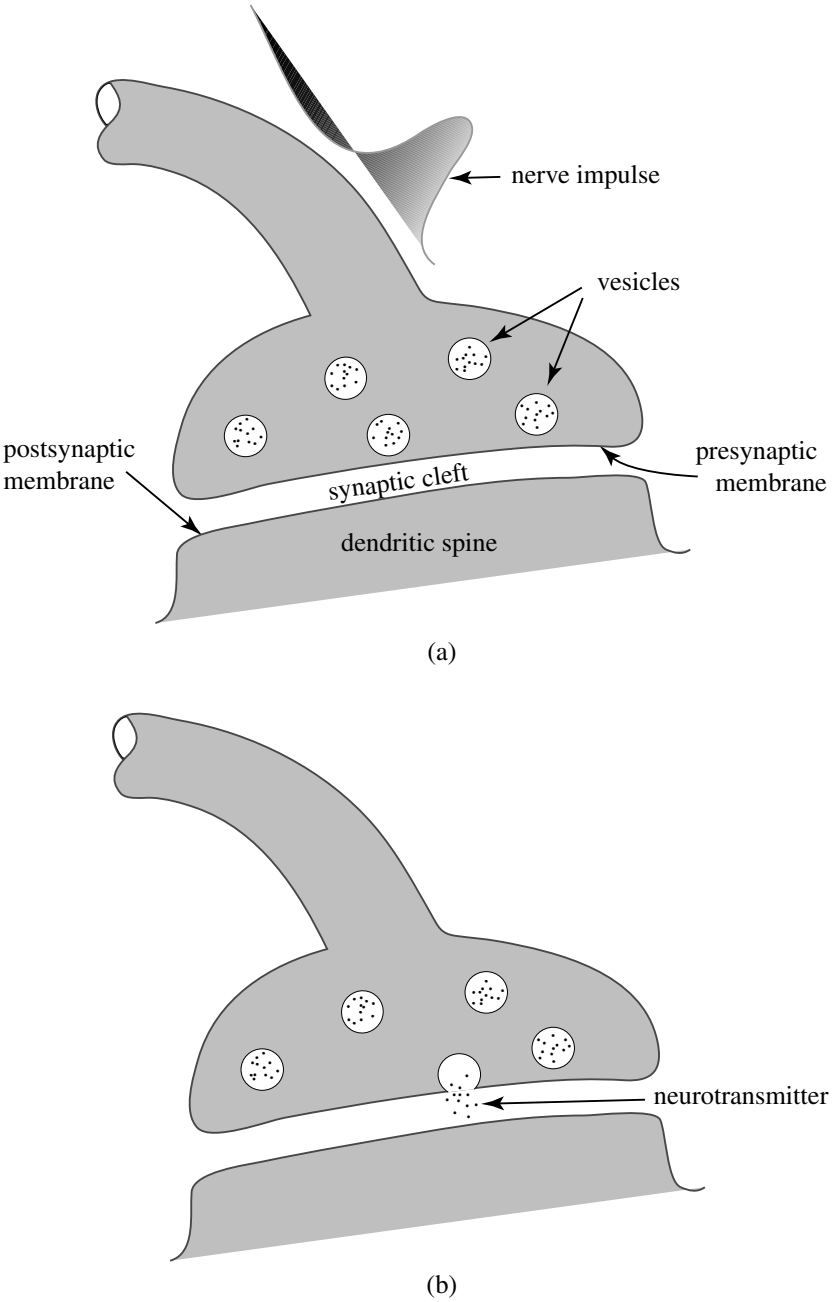

Figure 2.2. Sketches of a chemical synapse. (a) A nerve impulse arrives at the synapse, inducing a vesicle to fuse with the presynaptic membrane. (b) The process of exocytosis, wherein a vesicle is releasing its neurotransmitter molecules into the synaptic cleft. (The drawings are not to scale.)

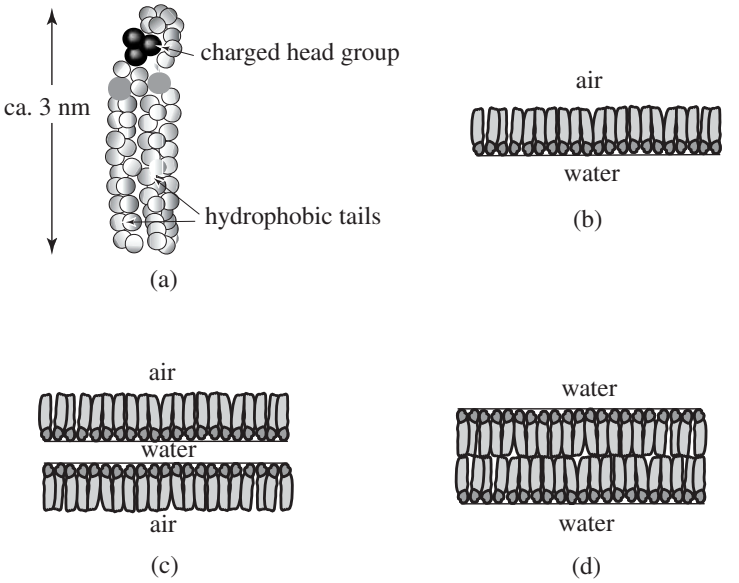

Figure 3.1. (a) A lipid (fatty) molecule (redrawn from Goodsell [3]). (b) A monomolecular lipid layer on water surface. (c) A bimolecular soap film. (d) A lipid bilayer.

bright light, you will at first observe the colored interference bands of the film that are familiar from childhood observations of soap bubbles. These color bands indicate that the film thickness is of the order of a wavelength of visible light ($\sim$ 4000 Å, or 400 nm) [1]. If you watch the film for a few minutes, however, it undergoes a dramatic change. Without breaking, the film becomes almost completely reflectionless, which indicates that its thickness has suddenly reduced to a value well below the wavelength of visible light, causing it to appear *black*. You are now observing a *bimolecular soap film* with the structure shown in Figure 3.1(c). (Within this film, a thin layer of water remains that attracts their charged head groups.)

Because the membrane of a biological cell is totally immersed in water, an energetically favorable structure is the lipid bilayer film, shown in Figure 3.1(d), and extended films can assume a variety of interesting geometries. If the film is a closed surface, for example, its natural form will be a sphere because that shape minimizes total energy, just as for soap bubbles.[2] Re-

[2]Collections of bubbles are yet more intricate. The next time you are washing up, you might take a careful look at a handful of soapsuds under a good light, noting that interior divisions tend toward a fourteen-sided figure, called a *tetrakaidekahedron* by Lord Kelvin. Just as the hexagon fills a two-dimensional area with a minimum boundary, this 14-gon is a space-filling shape with minimum wall area [19].

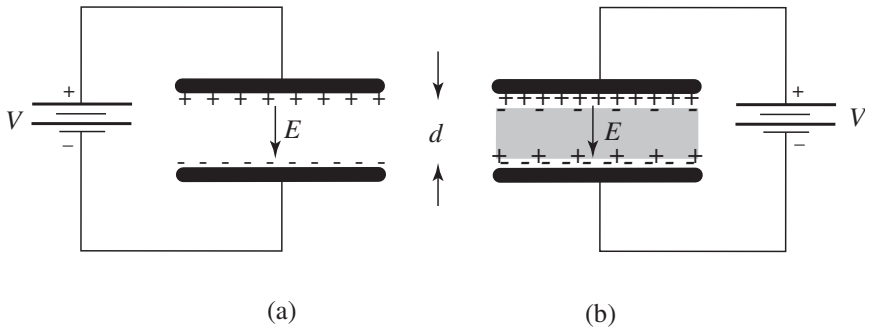

Figure 3.3. (a) A capacitor in a vacuum. (b) A capacitor that is filled with a material substance.

- The electrical capacitance of a lipid bilayer is about 1 microfarad (μF) per square centimeter.
- The electrical conductivity (or ionic permeability) of a pure lipid bilayer is very small, corresponding to that of a good insulator such as quartz.
- Membrane permeability is very sensitive to the presence of intrinsic proteins. If certain proteins are dissolved in the lipid bilayer, membrane conductivity increases by several orders of magnitude.
- With a proper choice of embedded membrane proteins, the switching action of a nerve membrane can be reproduced [10].

Because these observations are relevant to studies of the nerve, let us consider them in greater detail.

3.2 Membrane Capacitance

As we will see in the following chapter, the electrical capacitance of a nerve membrane plays a key role in the dynamics of its switching; thus, it is important for neuroscientists to understand what a capacitor is and the nature of the electric charge that it stores.

Consider first the vacuum capacitor shown in Figure 3.3(a) in which two parallel conducting plates of area A are separated by distance d. The plates are insulated from each other by a vacuum, so how does electric current manage to flow into the capacitor on the upper wire and out of it on the lower wire? Does electric current actually flow through the vacuum?

To answer such questions, let us connect a battery of voltage V across an uncharged capacitor with its positive (negative) terminal to the upper (lower) wire. Initially, current will flow into (out of) the upper (lower) plate,

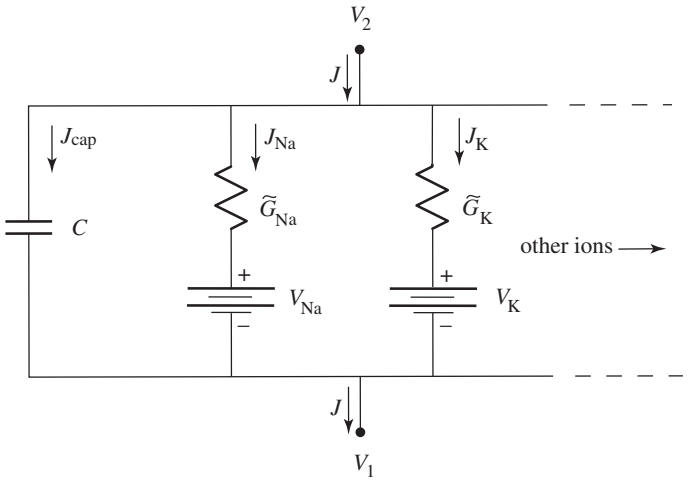

Figure 3.4. An electric circuit model for a unit area of the lipid bilayer membrane shown in Figure 3.2.

3.4 A Membrane Model

We are now in a position to assemble an electrical model for a lipid bilayer membrane that is permeable to an arbitrary number of ionic species, taking account of the following current components.

First, there is the capacitive component, which from Section 3.2 contributes a current density of

$$J_{\text{cap}} = C\frac{dV}{dt}\,,$$

where $C = \kappa\varepsilon_0/d$ is the capacitance per unit area of the bilayer. This current is represented as the left-hand branch in Figure 3.4, where in the context of Figure 3.2

$$V \equiv V_2 - V_1\,.$$

In addition to the capacitive current, there is also an ionic current for each species of ion that is able to pass through the membrane. Let us first consider the sodium ion current, which is represented as the second branch (counting from the left) in Figure 3.4.

From the previous section, sodium ion current consists of two independent components: conduction current (which flows in response to the voltage difference across the membrane) and diffusion current (which responds to the difference of sodium ion concentrations on the two sides of the membrane). Although they can be independently adjusted, these two components are linked by the Einstein relation between mobility and diffusion constant for each ion.

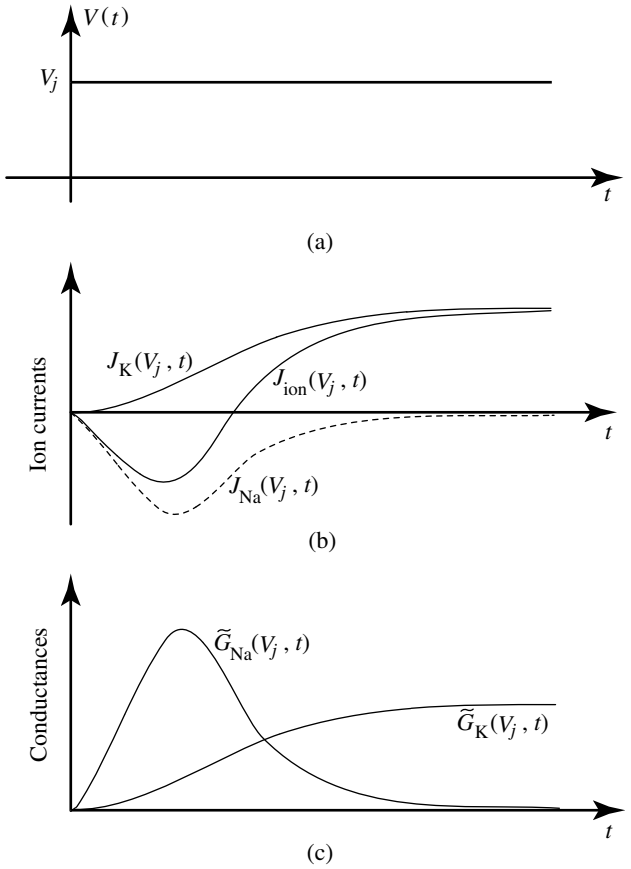

Figure 4.2. Figures related to the Hodgkin–Huxley determination of membrane conductances. (a) The applied voltage as a function of time. (b) Measurements of total ionic current and potassium current, from which sodium current can be calculated. (c) Sodium and potassium conductances at $V = V_j$ as functions of time. (See the text for details.)

where these diffusion potentials depend on the ratios of outside to inside ion concentrations.

To measure the individual (sodium plus potassium) components of membrane conductivity, Hodgkin and Huxley proceeded as follows [16].

(1) As indicated in Figure 4.2(a), the space-clamped membrane voltage was suddenly changed from the resting value ($V = 0$) at $t = 0$ to V_j, where

$$V_{Na} > V_j > 0\,,$$

and held there under voltage clamping. At this voltage, the total ion current, $J_{ion}(V_j, t)$, through the membrane was measured as a function of time,

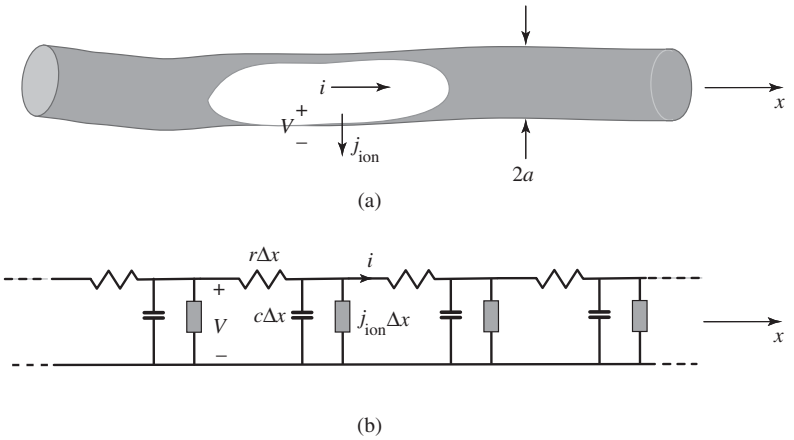

Figure 4.3. (a) Sketch of a squid axon. (b) A corresponding differential circuit diagram that can be used to derive the cable equation for impulse propagation.

where i is the longitudinal (x-directed) current flowing through the nerve. From conservation of electric charge, we also know that to first order in Δx

$$i(x,t)-i(x+\Delta x,t) = \left(c\frac{dV(x+\Delta x/2,t)}{dt} + j_{\rm ion}(x+\Delta x/2,t)\right)\Delta x\,. \quad (4.9)$$

Combining these two equations to eliminate i and taking the limit as $\Delta x \to 0$ yields the following *nonlinear diffusion equation*:

$$\frac{1}{rc}\frac{\partial^2 V}{\partial x^2} - \frac{\partial V}{\partial t} = \frac{j_{\rm ion}}{c}\,. \quad (4.10)$$

Motivated by familiarity with a related partial differential equation that arose in the analysis of telegraph lines, Equation (4.10) is often called the "cable equation" by electrophysiologists, but this name is misleading. Propagation of dits and dahs over a telegraph line is a linear electromagnetic phenomenon, whereas Equation (4.10) represents *nonlinear* electrostatic diffusion.[6]

From the perspectives of modern nonlinear science, Equation (4.10) is a *nonlinear field equation* out of which emerges an elementary particle of neural activity: the nerve impulse [35]. It is nonlinear because of the nonlinear dependencies of $j_{\rm ion}$ on m, h, and n, which in turn depend nonlinearly on V.

Let us now analyze the cable equation to understand how a nerve impulse emerges from the mathematical structure that we have developed.

[6]Using Maxwell's equations, one can take magnetic effects into account in the derivation of Equation (4.10), but the error involved in neglecting this correction is about one part in 10^8 [33].

to zero with increasing time as solutions of the full PDE given by Equation (4.10). (See Sections 5.4 and 6.5.2 and Appendix D for discussions of nerve impulse stability criteria.)

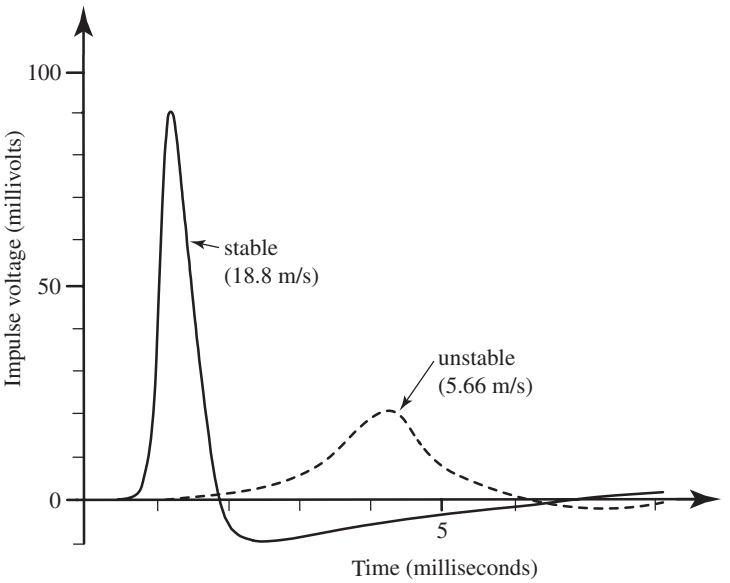

Figure 4.5. A full-sized spike (at $v = 18.8$ m/s) and an unstable threshold impulse (5.66 m/s) for the Hodgkin–Huxley axon at 18.5°C. (Redrawn from Huxley [21].)

The smaller-amplitude traveling wave solution, with a speed of 5.66 m/s, was found by Huxley in 1959 using an electronic computing machine [21]. This solution is *unstable* in the sense that deviations from it diverge with increasing time as solutions of the full PDE given by Equation (4.10). Slightly smaller solutions decay to zero, and slightly larger solutions grow to become the fully developed nerve impulse; thus, this unstable solution defines *threshold conditions* for igniting an impulse.

In the language of modern nonlinear theory, the stable traveling wave of greater amplitude can be viewed as an *attractor* in the solution space of the PDE system of Equation (4.10); thus, solutions lying within a *basin of attraction* converge to the attractor as $t \to +\infty$. The lower-amplitude unstable solution, on the other hand, lies on a *separatrix* dividing an impulse's basin of attraction from that of the null solution.

4.6 Degradation of a Squid Nerve Impulse

By the middle of the 1960s, electronic computing machines had developed to a level where the original Hodgkin–Huxley calculations were fairly

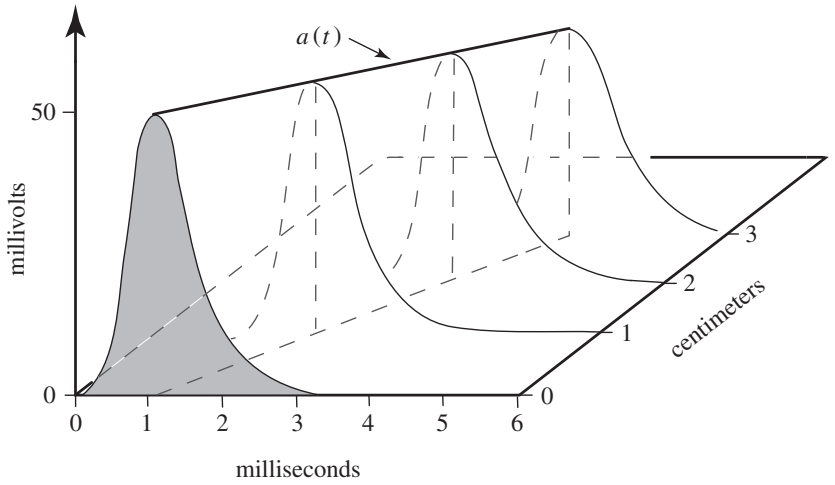

Figure 4.7. Decremental propagation of an impulse on an H–H axon that is narcotized by the factor $\eta = 0.25$ (sketched from data in [9] and [25]).

where the two solutions merge. For yet smaller values of η, no traveling-wave solutions exist.

To appreciate the physical significance of these results, look at the (v, η) parameter plane of Figure 4.6. The curve plotted in this plane shows the loci of parameters where a balance is established between the rate at which energy is generated by the ionic batteries in Equation (4.5) and the rate at which it is dissipated by the ionic currents associated with a nerve impulse.

The upper curve indicates stable traveling-wave solutions, implying that a small change of an impulse solution (either positive or negative) will relax back to zero and restore the original wave. The lower curve indicates unstable traveling waves, implying two different effects. An increase in amplitude of the solution will grow (because energy generation is greater than dissipation) until the total solution reaches the stable solution of the upper curve. If its amplitude is decreased, on the other hand, the impulse will decay (because energy generation is less than dissipation) until it falls to zero. These numerical results provide an explanation for the *all-or-nothing* property of a nerve impulse noted by Adrian in 1914 [2].

Although the concept of all-or-nothing propagation holds for $\eta > \eta_c$, its logical basis evaporates for $\eta < \eta_c$. In this regime, however, one can find *decremental* propagation of a nerve impulse, as is sketched in Figure 4.7 [9, 25]. For such a decremental impulse, the rate at which energy is generated is only slightly less than the rate of dissipation, so the solution relaxes rather slowly to zero. As has been emphasized by Lorente de Nó and Condouris [27], this phenomenon was long overlooked by electrophysiologists who had concentrated their attentions on the properties of standard nerves.

These qualitative conclusions stemming from the computations of Cooley and Dodge are quite general, applying to several other experimental

5
Leading-Edge Models

To develop an intuitive understanding of a challenging area, it is sometimes useful to bracket the problem, on one hand looking fully at the intricacies and on the other taking the simplest possible perspective. Having considered a rather complete description of a squid axon in Chapter 4, we now turn our attention to simpler models of a nerve fiber that focus attention on the *leading edge* of an impulse.

Although lacking the scope and precision of the Hodgkin–Huxley formulation, these models are easier to grasp and thus useful for appreciating some fundamental aspects of nerve impulse propagation, including stability. Furthermore, we will obtain analytic expressions for impulse velocity and threshold conditions for impulse ignition and show how these features depend on physical parameters of the nerve.

5.1 Leading-Edge Approximation for the H–H Impulse

As we learned in the previous chapter, propagation in a Hodgkin–Huxley squid axon is governed by the nonlinear diffusion equation (or "cable equation") given in Equation (4.10), where j_{ion} is the ionic current flowing out of the fiber per unit of distance in the x-direction. This ionic current, in turn, has three components: sodium, potassium, and leakage.

Because the time for turn-on of the sodium current is about an order of magnitude shorter than the times for sodium turn-off and potassium turn-on, an attractive approximation for representing the leading edge of

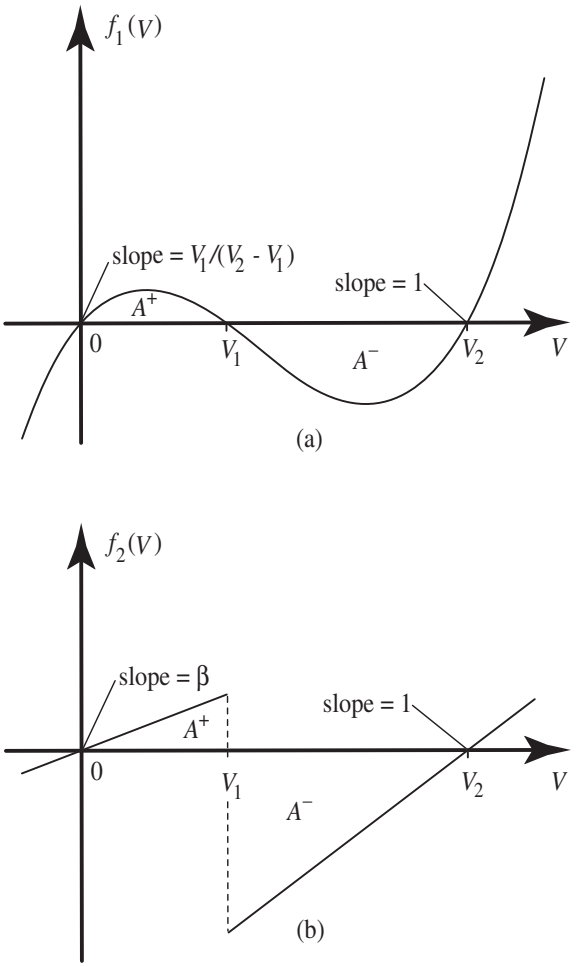

Figure 5.3. Two forms of the function $f(v)$ for which Equation (5.5) has analytic traveling-wave solutions. (a) A cubic function defined in Equation (5.9). (b) A piecewise linear function defined in Equation (5.12).

as can be checked by direct substitution. (In these equations, there is no tilde on v because the velocity is no longer in normalized units.)

2. *Piecewise linear model:* Shortly after the observation by Cole and Curtis that the impedance of a squid membrane decreases by a factor of about 40 during the passage of a nerve impulse [2], Offner, Weinberg, and Young proposed to model a nerve membrane by the "piecewise linear" conductance shown in Figure 5.3(b) and defined by [11]

6
Recovery Models

Propagation of a nerve impulse is often compared with the burning of a candle, of which the leading-edge models considered in the previous chapter provide examples. This is a flawed metaphor, however, because a candle burns only once, spending (like H.C. Andersen's little match girl) its entire store of chemical energy to keep the flame bright and hot, with no possibility of transmitting a second flame. As we have seen both from Cole's classic oscillogram of Figure 1.1 and the more detailed data of Figure 4.8, a nerve impulse exhibits *recovery* over an interval of a few milliseconds, allowing subsequent impulses to be transmitted by the nerve. Without this feature, our nervous systems would be useless for processing information, and the animal kingdom could not have developed.

In this chapter, we explore some simple models for the recovery phenomenon that are useful not only for broadening our physical and mathematical understanding of nerve impulse propagation but also for making better estimates of nerve behavior.

6.1 The Markin–Chizmadzhev (M–C) Model

One of the simplest means for representing recovery of a propagating nerve impulse was introduced by Kompaneyets and Gurovich in the mid-1960s [23] and developed in detail by Markin and Chizmadzhev in 1967 [24]. This M–C model assumes the diffusion equation (or "cable equation") with which we began the previous chapter; thus the transmembrane voltage V

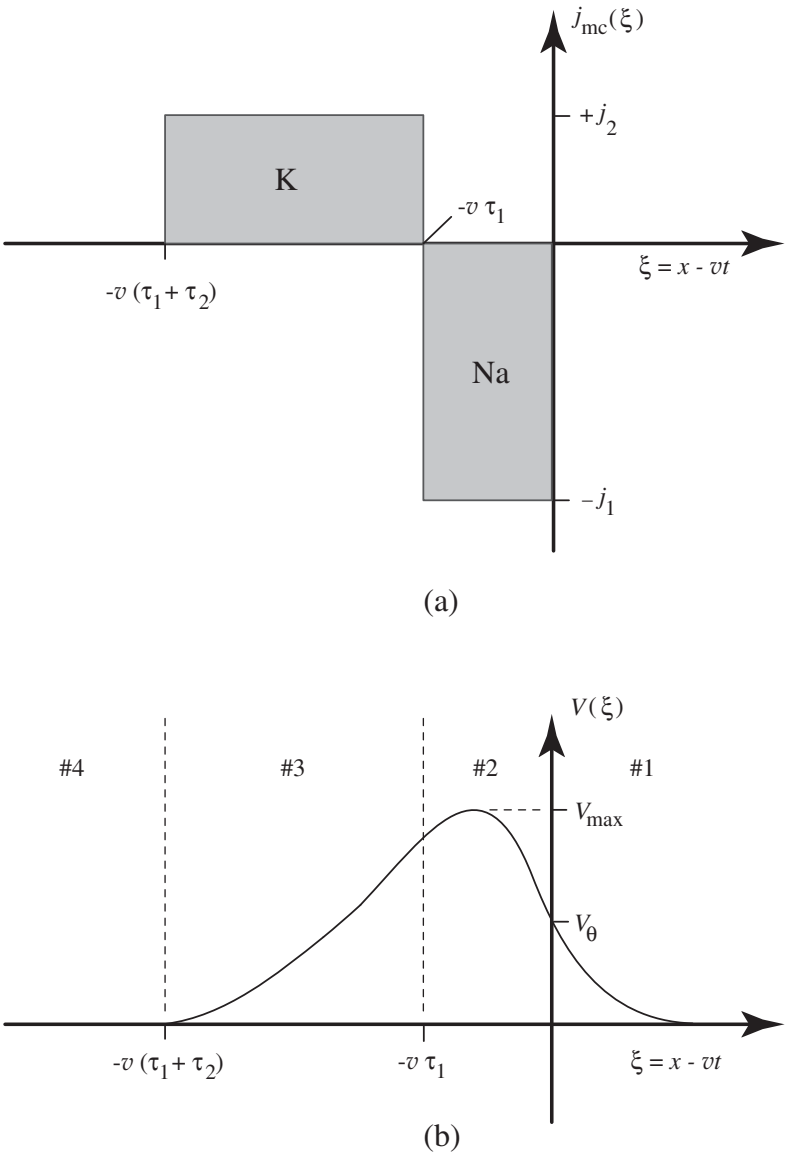

Figure 6.1. (a) Ionic current in the M–C model as a function of the traveling-wave variable (ξ). (b) Structure of the associated nerve impulse.

- Because $V_4(\xi) = 0$ and $V_1(\xi) = C_1 \exp(-vrc\xi)$, there are a total of seven constants to determine: C_1, A_2, B_2, C_2, A_3, B_3, and C_3. (The impulse speed v appears as a parameter in Equation (6.5), so these "constants" are actually functions of the traveling-wave speed.) The boundary conditions between regions #1 and #2, #2 and #3, and #3

is governed by the PDE[1]

$$\frac{1}{rc}\frac{\partial^2 V}{\partial x^2} - \frac{\partial V}{\partial t} = \frac{j_{\rm mc}(x,t)}{c}\,. \tag{6.1}$$

In this model, however, the ionic membrane current is not represented as a voltage-dependent variable, as in Equation (5.3), but by one of the following prescribed functions of time.

(1) If V does not reach the threshold value of V_θ, then

$$j_{\rm mc}(x,t) = 0\,.$$

(2) If, on the other hand, V does reach the threshold value of V_θ at some instant (which is defined as $t = 0$), then at $x = 0$

$$\begin{aligned} j_{\rm mc}(0,t) &= 0 \quad \text{for} \quad t < 0\,, \\ &= -j_1 \quad \text{for} \quad 0 < t < \tau_1\,, \\ &= +j_2 \quad \text{for} \quad \tau_1 < t < \tau_1 + \tau_2\,, \text{ and} \\ &= 0 \quad \text{for} \quad t > \tau_1 + \tau_2\,. \end{aligned} \tag{6.2}$$

Whereas Equation (5.2) is a nonlinear diffusion equation, Equation (6.1) is a *piecewise linear inhomogeneous diffusion equation,* which is easier to solve. Thus, this is evidently a helpful assumption to make, but how do we choose the parameters $(j_1, j_2, \tau_1, \tau_2)$ that define $j_{\rm mc}(0,t)$?

Recalling that the positive direction for ionic current is outward, the early current $-j_1$ represents the inward flow of sodium ions, whereas the later component $+j_2$ describes outward flow of potassium ions. Thus, τ_1 and τ_2 can be obtained from the waveform of the squid impulse in Figure 1.1, and it is possible to estimate j_1 from the leading-edge charge Q_0, which we obtained in Equation (5.20).

Noting that j_1 has the units of current per unit of distance along the axon (amperes per centimeter), it follows that the spatial width over which inward current flows is $v\tau_1$, where v is the impulse speed. Assuming further that the flow of j_1 across the membrane supplies the leading-edge charge—defined in Equation (5.19)—implies $j_1 v\tau_1 = Q_0/\tau_1$, or

$$j_1 = \frac{Q_0}{v\tau_1^2} = \frac{Q_0^2 r}{V_{\max}\tau_1^2} \ \ \text{A/cm}\,. \tag{6.3}$$

Finally, the condition

$$j_1\tau_1 = j_2\tau_2$$

[1] An even simpler version of the M–C concept is the "integrate and fire" model of a neuron, in which the entire cell is approximated as a single switch in parallel with a capacitor [1, 21, 22]. The capacitor integrates incoming charge until a threshold voltage is reached, whereupon the switch closes briefly, discharging the capacitor and restarting the process. A more realistic version is Gerstner's "spike response model" [12, 13], which is convenient for approximate numerical studies of large neural networks.

7
Myelinated Nerves

Following the Hodgkin–Huxley formulation of nerve impulse dynamics for the giant axon of the squid [31], most mathematical studies have focused on smooth nerve fibers, as in the previous three chapters. Although this picture is appropriate for the squid axon, many vertebrate nerves—including the frog motor nerve studied by Galvani and axons of mammalian brains—are bundles of discrete, periodic structures, comprising active nodes (also called "nodes of Ranvier") separated by relatively long fiber segments that are insulated by a fatty material called myelin. In such *myelinated* nerves, the wave of activity jumps from one node to the next, and should be modeled by nonlinear difference-differential equations rather than by PDEs.

Impulse propagation on myelinated nerves (called *saltatory* conduction by the electrophysiologists) is qualitatively similar to a row of falling dominos or to the signal fires of coastal warning systems during the Middle Ages. In an evolutionary context, myelinated nerve structures are useful because they allow an increase in the speed of a nerve impulse while decreasing the diameter of the nerve fiber. Thus, the motor nerves of vertebrates may comprise several hundred individual saltatory fibers, each serving as an independent signaling channel [76]. The rabbit sciatic nerve shown in Figure 1.2, for example, can transmit information about three orders of magnitude faster than a squid axon of the same diameter while expending much less energy in transmitting an individual impulse than does a smooth fiber.

Over the past century, studies of impulse propagation on myelinated nerves have been carried on in three different professional areas, among which there has been less than ideal communication. Electrophysiology, of course, is the foremost of these groups [7, 11, 33, 35, 61, 62, 68, 69], and since

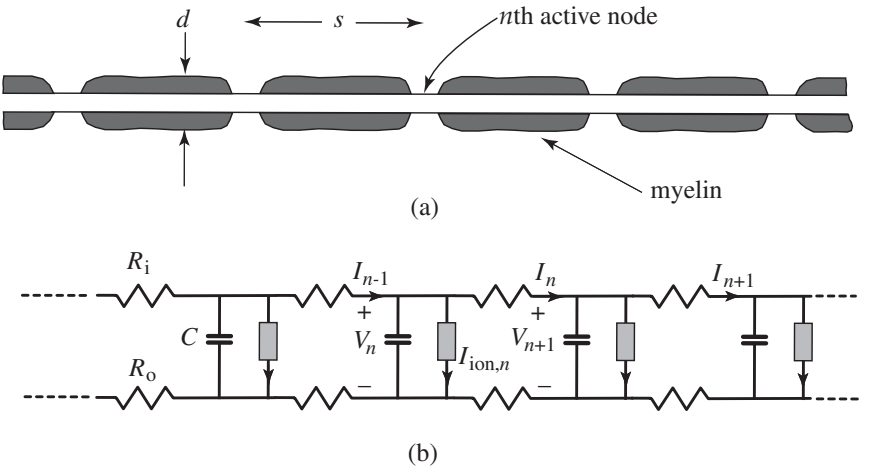

Figure 7.1. (a) A single myelinated nerve fiber (not to scale). (b) The corresponding electric circuit diagram.

for which a corresponding electric circuit diagram is shown in Figure 7.1(b).[1]

In these equations, the index n indicates successive active nodes, each characterized by a transverse voltage across the membrane (V_n). A second dynamic variable is the current (I_n) flowing longitudinally through the fiber from node n to node $n + 1$. Thus Equation (7.1) is merely Ohm's law, which relates the voltage difference between two adjacent nodes of the current flowing between them times the sum of the inside and outside resistances, R_i and R_o.

Equation (7.2) says that the current flowing into the nth node from the $(n - 1)$th node (I_{n-1}) minus the current flowing out of it to the $(n + 1)$th node (I_n) is equal to the following two components of transverse (inside to outside) current leaving the node: capacitive current, $C\,dV_n/dt$, and ionic current, $I_{ion,n}$, comprising mainly a sodium component [31].

The time delay for the onset of sodium ion permeability is rather short (in the frog nerve it is about 0.1 ms), whereas the time delay for the on-

[1]More correctly, the passive fiber joining two active nodes should be represented by a linear diffusion equation (see Section 9.1.1), as was approximately done by Moore et al. [48]. In Equations (7.1) and (7.2), however, the passive internode fiber is modeled by a single series resistance (R_i) and a single shunt capacitor (equal to the capacitance of the myelin sheath), which is simply added to the node capacitance to obtain the total capacitance C. Although this approximation neglects shunt conductance of the myelin sheath, Moore et al. have shown that it has a negligible effect on conduction velocity. Such a "Π-network approximation" for the internode fiber greatly eases computational problems while reducing the number of parameters to be considered, thereby facilitating interpretations of numerical results.

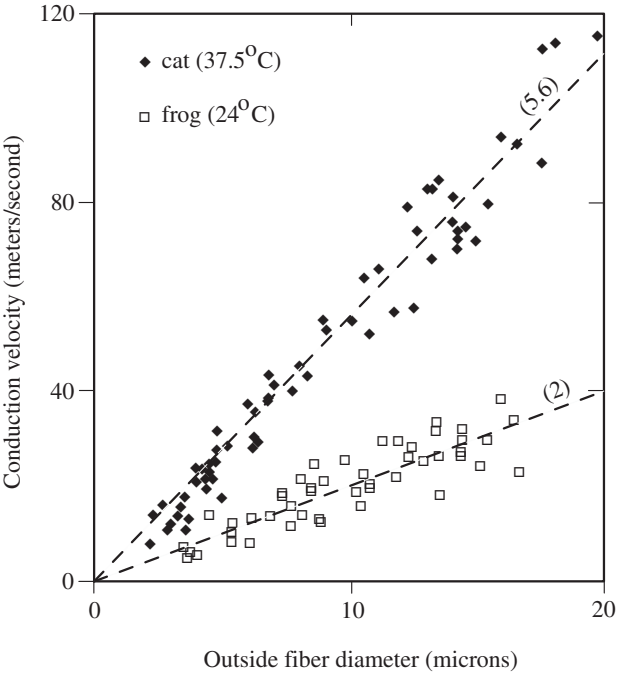

Figure 7.3. Empirical conduction velocities (v_e) vs. outside fiber diameters (d) for myelinated axons of two different vertebrate species: the frog at a temperature of 24°C (from data in [71]), and the cat at a temperature of 37.5°C (from data in [33]).

outer fiber diameter of 14 μm, the calculated conduction velocity of 29 m/s is in accord with the data of Figure 7.3.

Assured that the simple model of Section 7.1 is not unreasonable, we are led to two observations of biological significance. First, failure of an impulse on the standard frog axon is expected to occur at an internode spacing of 9.5 mm (corresponding to $D^* = 0.21$), whereas the normal spacing is 2 mm. The evolutionary design of this axon thus provides a comfortable margin of safety against failure. Second, Figure 7.2 shows that at $D = 1$ the impulse velocity of a normal frog nerve is close to the maximum possible value, again suggesting that an optimal design has evolved.

Although the preceding results for varying D (or internode spacing $s = 2\,\text{mm}/D$) have been obtained under the assumption that other properties of a nerve fiber remain fixed, this is a mathematical fiction. In real nerves, some sort of design optimization has occurred over the course of biological evolution that simultaneously adjusts all parameters in appropriate ways.

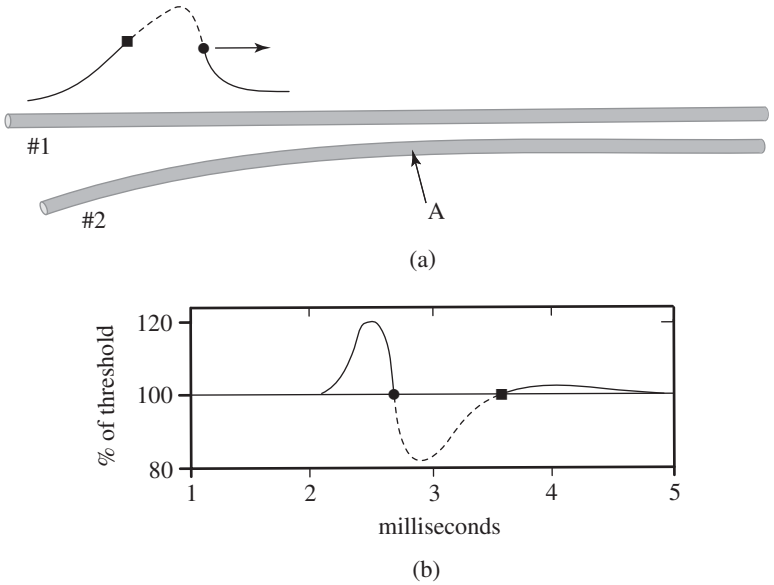

Figure 8.1. (a) Experiment of Katz and Schmitt to measure impulse interactions on parallel fibers. (b) Change in threshold on fiber #2 (at point A) caused by the presence of an impulse on fiber #1. (Redrawn from [17].)

pioneering work of Arvanitaki [1] inspired several observations of ephaptic interactions [4, 10, 12, 14, 17, 18, 19, 25, 26, 28, 29]. More recent references include both theoretical and experimental studies [2, 7, 8, 11, 27] and the important review by Jefferys [15].

An early investigation by Katz and Schmitt provides particularly clear evidence for nonsynaptic interactions [17, 18, 19]. From a variety of experiments on a pair of naturally adjacent, unmyelinated fibers from the limb nerve of a crab, these authors presented the following results.

- Using the experiment sketched in Figure 8.1(a), a reference impulse was launched on fiber #1 from the left, traveling toward the right, and at various later times the relative threshold on fiber #2 was measured at point A.
  Their observations are sketched in Figure 8.1(b), from which it is seen the threshold on fiber #2 changes in a manner that is related to the second derivative of the impulse voltage on fiber #1. (To emphasize this relationship, the impulse voltage in Figure 8.1(a) is dashed where its second derivative is negative, and the corresponding range of reduced threshold in Figure 8.1(b) is also dashed.)

- If impulses are launched at about the same time on two parallel fibers with independent impulse speeds that do not differ by more than

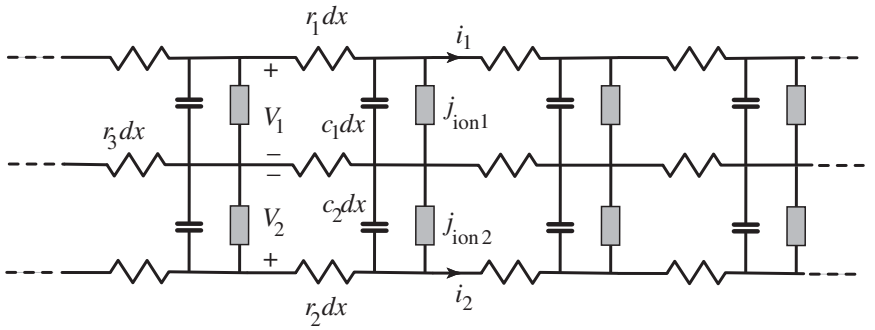

Figure 8.2. Markin's equivalent circuit for two ephaptically coupled nerve fibers [22, 23].

the late 1970s using internal and external voltage recordings to obtain data confirming the second of Equations (8.2). Although ephaptic interactions are unlikely to permit direct transmission of an impulse from one nerve fiber to another, they concluded, impulse coupling is feasible under normal physiological conditions.

Key to the M–C description of nerve impulse propagation is the assumption that

$$j_{\text{ion}} = j_{\text{mc}}(\xi)\,,$$

where $j_{\text{mc}}(\xi)$ follows the piecewise constant function shown in Figure 6.1 whenever V reaches the threshold voltage. Thus, any influence that reduces (increases) the time for an impulse to reach threshold will increase (decrease) its speed.

To apply this concept, let us assume that an impulse on fiber #2 is *leading* an impulse on fiber #1 by a distance δ. In other words, the impulse on fiber #1 goes through threshold at $\xi_1 = 0$, where

$$\xi_1 = x - v_1 t\,,$$

and the impulse on fiber #2 goes through threshold at $\xi_2 = 0$, where

$$\xi_2 = x - v_2 t - \delta\,.$$

Now note two additional facts that are evident from the general shape of a nerve impulse: (i) ahead of the point where an impulse goes through threshold, its second space derivative is positive; and (ii) behind this point the second space derivative is negative.

Consider the first of Equations (8.1), and assume that $\xi_1 \approx 0$. Because V_2 has already gone through its threshold, $\partial^2 V_2/\partial x^2$ is negative. Thus, the influence of V_2 on impulse #1 is to increase $\partial V_1/\partial t$, thereby raising V_1 above what it would be without the interaction. This has the effect of speeding up impulse #1 (increasing v_1), which causes δ to decrease.

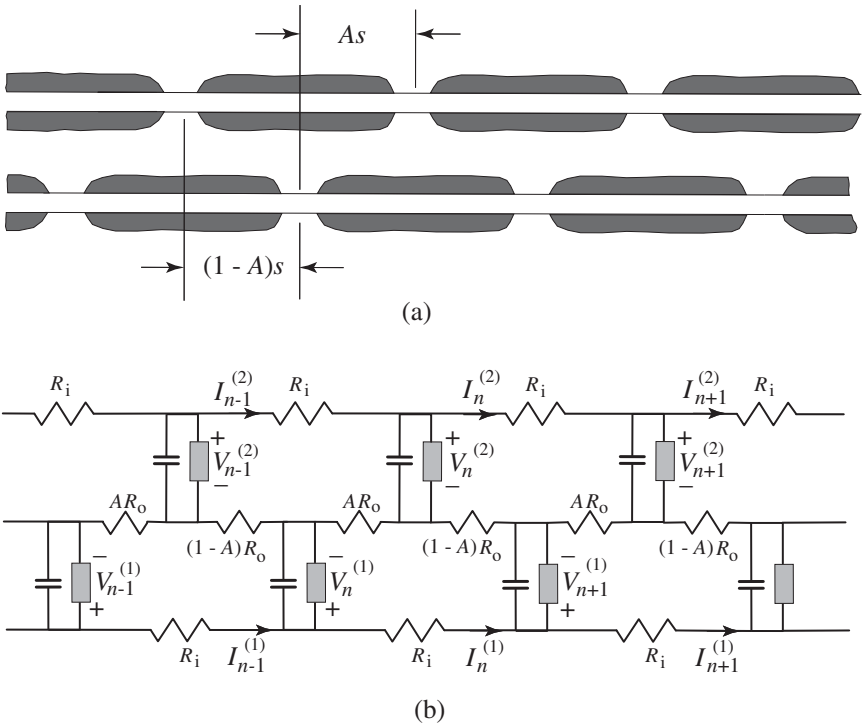

Figure 8.6. (a) Two myelinated nerves on which impulses may be coupled by a linking of their external return currents (not to scale). (b) A circuit diagram of the coupled myelinated nerves.

determined by the $I_n^{(1)}$ and $I_n^{(2)}$.) Equating the voltages about the meshes to zero leads directly to the equations

$$\begin{aligned} V_n^{(1)} - V_{n+1}^{(1)} &= (R_i + R_o)I_n^{(1)} + R_o\left[AI_n^{(2)} + (1-A)I_{n-1}^{(2)}\right], \\ V_n^{(2)} - V_{n+1}^{(2)} &= (R_i + R_o)I_n^{(2)} + R_o\left[AI_n^{(1)} + (1-A)I_{n+1}^{(1)}\right], \end{aligned}$$

where the voltages across the active nodes are related to the mesh currents by

$$I_{n-1}^{(j)} - I_n^{(j)} = C\frac{dV_n^{(j)}}{dt} + I_{\text{ion},n}^{(j)}.$$

As in the previous chapter, it is analytically convenient to model the ionic current in the cubic approximation

$$I_{\text{ion},n}^{(j)} = \left(\frac{G}{V_2(V_2 - V_1)}\right) V_n^{(j)}(V_n^{(j)} - V_1)(V_n^{(j)} - V_2),$$

which was introduced in Equation (5.9).

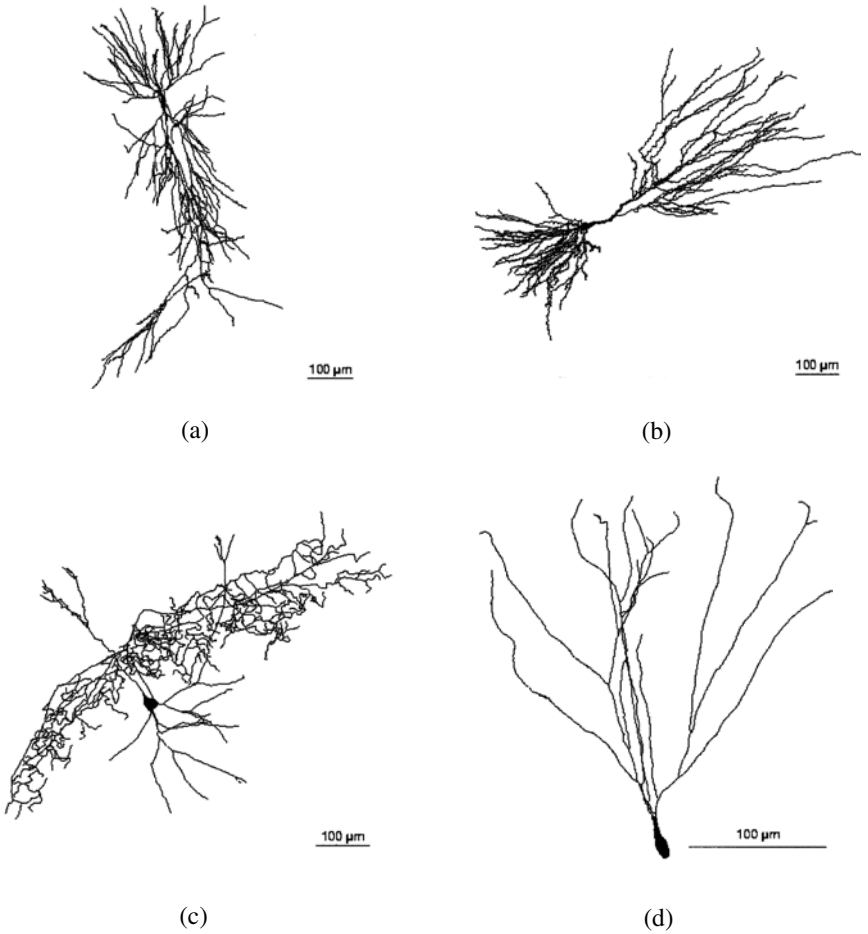

(a) (b)

(c) (d)

Figure 9.1. Typical dendritic trees in the hippocampus of the rat. (a) CA1 pyramidal cell [90]. (b) CA3 pyramidal cell [127]. (c) Interneuron [76]. (d) Granule cell [128]. (From the Southampton–Duke Public Morphological Archive [27].)

fiber, which is more than an order of magnitude smaller than the active conductance (g) that was considered in Chapter 5.

It is convenient to normalize this equation by measuring time in units of $c/g_{\rm rest}$ and distance along the fiber in units of $1/\sqrt{rg_{\rm rest}}$. Then Equation (9.1) reduces to the normalized form

$$\frac{\partial^2 V}{\partial \tilde{x}^2} - \frac{\partial V}{\partial \tilde{t}} = V\,, \tag{9.2}$$

where

$$\tilde{x} \equiv x\sqrt{rg_{\rm rest}} \quad \text{and} \quad \tilde{t} \equiv t\frac{g_{\rm rest}}{c}\,.$$

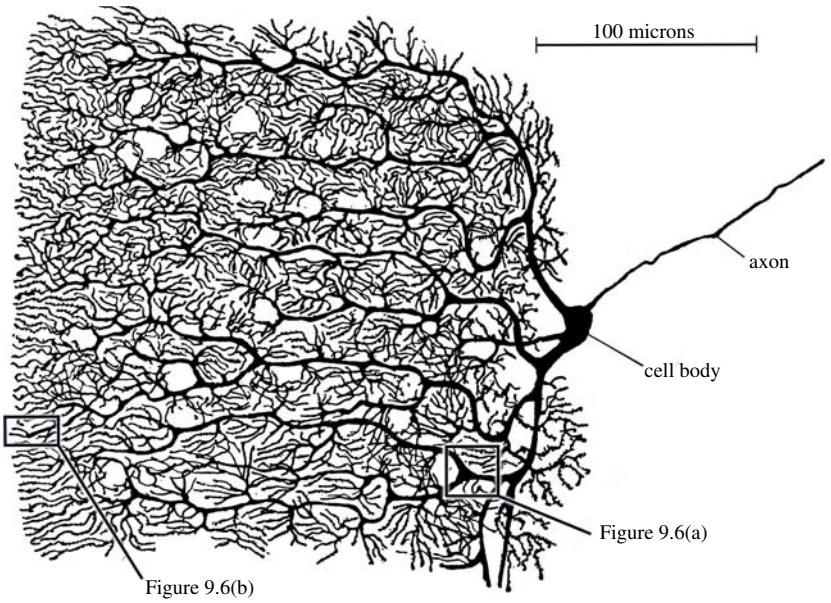

Figure 9.5. Ramón y Cajal's classic image of a Purkinje cell from the human cerebellum [96].

blocking condition is satisfied. To this end, let us consider the bifurcation shown in Figure 9.4(b) with the notation that d_1 and d_2 are daughter diameters and d_3 is the diameter of the parent branch. Extracted and enlarged from Figure 9.5, two possibilities are indicated in Figure 9.6.[6]

OR *Bifurcations*
For the simple branch shown in Figure 9.6(a), it is seen that $d_1 \approx d_2 \approx d_3$. Supposing that an impulse arrives at the branch from (say) daughter #1,

$$\frac{d_2^{3/2} + d_3^{3/2}}{d_1^{3/2}} \approx 2\,.$$

All of the models treated in the preceding section imply that this GR is too small for blocking of an impulse to occur. Thus incoming impulses on either of the two daughters are able to ignite the parent. Using the jargon of computer engineering, this can be described as an OR junction because

[6]The examples given in this section are for illustration only because the Golgi stain technique used by Ramón y Cajal to obtain Figure 9.5 may not record all of the dendritic structures.

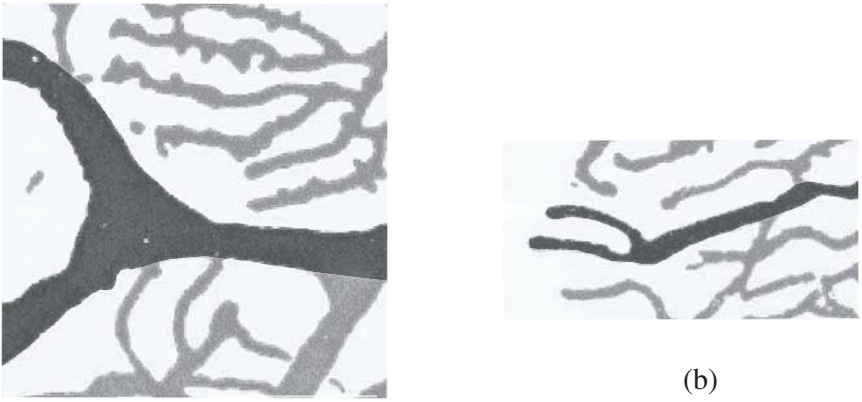

(a) (b)

Figure 9.6. Details of the Purkinje cell branchings indicated in Figure 9.5. (a) An OR bifurcation. (b) A possible AND bifurcation.

an input on one "or" the other daughter is sufficient to ignite the parent fiber.

In evaluating the computational utility of this OR bifurcation, one should note that an incoming impulse on one daughter will launch an outward-going impulse on the other daughter, disabling that daughter's segment of the dendritic tree for a certain interval of time [107, 132].

AND *Bifurcations*

Computer engineers use the term "AND junction" to describe an element for which inputs on both the first input "and" the second input acting together are required to produce an output signal, implying that one input acting alone is insufficient to produce an output.

If it is assumed that the dendritic trees are composed of Hodgkin–Huxley fibers that support fully developed impulses, the condition for failure of a single incoming impulse is

$$\frac{d_2^{3/2} + d_3^{3/2}}{d_1^{3/2}} > 12.7\,.$$

From an examination of the various geometric configurations in the dendritic trees of the Purkinje cell in Figure 9.5, it is difficult to find branchings that satisfy this condition. One of the more promising candidates is shown in Figure 9.6(b), from which it is seen that the parent branch diameter (d_3) is about 2.5 times those of the incoming daughter branches (d_1 and d_2). Thus

$$\frac{d_2^{3/2} + d_3^{3/2}}{d_1^{3/2}} \approx 5\,,$$

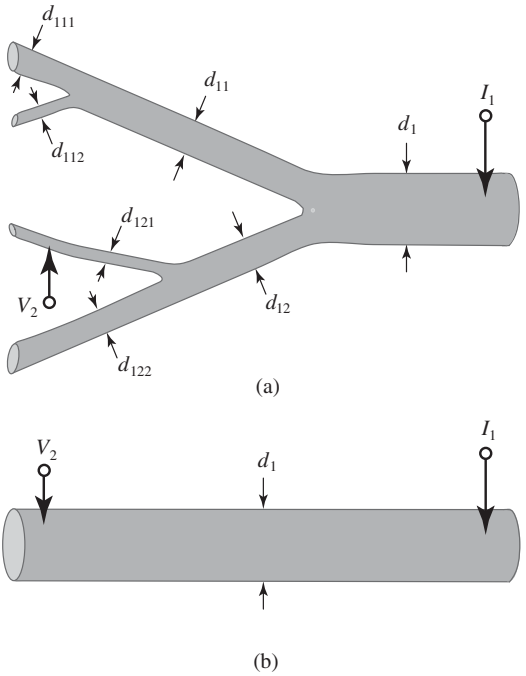

Figure 9.3. (a) A branching dendritic structure. (b) Rall's "equivalent cylinder" for the structure in (a).

task; thus, it is of interest to consider an unexpectedly simple case introduced by Wilfred Rall in 1959 [92, 93, 94, 95]. To see how this goes, refer to Figure 9.3(a), which represents an arbitrary dendritic branching region.

Suppose that a steady current I_1 is injected into the large fiber at location #1 on the left-hand side of the diagram from which the resulting steady transmembrane voltage V_2 is to be computed at location #2 on one of the smaller branches. Although time derivatives have been neglected, this remains a difficult calculation because a discontinuity (or *reflection*) in the solution occurs at each branching (or *bifurcation*) in Figure 9.3(a). Dealing with reflections is not a new problem; radio, microwave, acoustic, and optical engineers have long been interested in doing so in order to increase the efficiencies of electromagnetic, sound, or light transmissions. How do they accomplish this?

To minimize reflections, the standard procedure is to make the *characteristic admittance* (Y_0) of the transmission system equal on both sides of a boundary, where

$$Y_0 \equiv \sqrt{\frac{\text{shunt admittance/length}}{\text{series impedance/length}}}\,.$$

or absent), the three basic operations of Boolean arithmetic are:

$$\left[\begin{array}{lcl} 1 \text{ AND } 1 & = & 1 \\ 1 \text{ AND } 0 & = & 0 \\ 0 \text{ AND } 1 & = & 0 \\ 0 \text{ AND } 0 & = & 0 \end{array}\right], \left[\begin{array}{lcl} 1 \text{ OR } 1 & = & 1 \\ 1 \text{ OR } 0 & = & 1 \\ 0 \text{ OR } 1 & = & 1 \\ 0 \text{ OR } 0 & = & 0 \end{array}\right], \text{ and } \left[\begin{array}{lcl} \text{NOT } 1 & = & 0 \\ \text{NOT } 0 & = & 1 \end{array}\right].$$

In the context of this arithmetic, a Boolean function specifies the output variable for each combination of input variables. Thus a particular Boolean function of three inputs A, B, and C might be denoted as $F(A, B, C)$ and defined as in the following table.

A	B	C	$F(A, B, C)$
0	0	0	0
0	0	1	0
0	1	0	0
0	1	1	0
1	0	0	0
1	0	1	1
1	1	0	0
1	1	1	1

A Boolean expression for this particular function is

$$\begin{aligned} F(A, B, C) &= (A \text{ AND } B \text{ AND } C) \text{ OR} (A \text{ AND NOT } B \text{ AND } C) \\ &= A \text{ AND } C \end{aligned} \tag{10.1}$$

indicating in ordinary English that an output impulse will appear if either of two input conditions occurs: there are impulses at A, B, and C, or there are impulses at A and at C but not at B. In this formulation, "at" refers to a location in space-time because the AND operation requires temporal coincidence.

Because a Boolean function of N inputs has 2^N input combinations for which the corresponding output is either 0 or 1, there are evidently

$$2^{2^N}$$

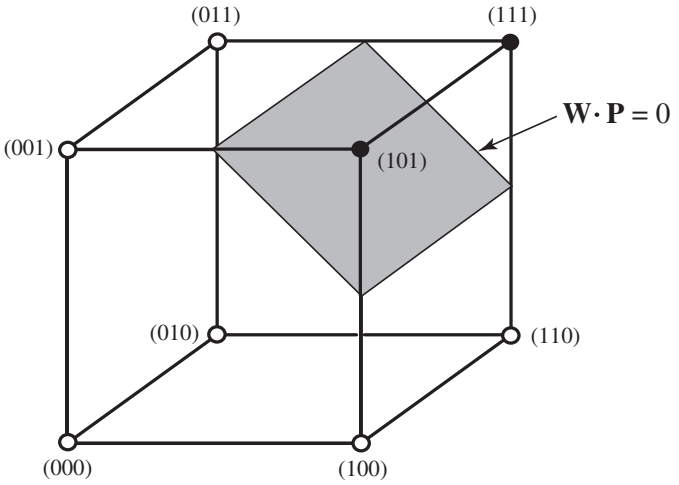

Figure 10.1. The geometrical interpretation of the pattern-recognition task indicated by Equations (10.1) and (10.3).

the barometer is rising and $A = 0$ that it is falling, $B = 1$ implies daytime and $B = 0$ night, and $C = 1$ indicates that it is clear and $C = 0$ indicates cloudiness. With $F(A, B, C)$ defined as in Equation (10.1), it is reasonable to expect that $F = 1$ implies that no rain is to be expected within the next few hours.

To understand how the training algorithm works, it helps to view pattern-recognition problems in a geometrical context. Thus, the eight values of these three input variables can be taken as vertices of a cube, as indicated in Figure 10.1, with the black dots indicating where $F = 1$ and the open dots where $F = 0$. The shaded area indicates a *linear discriminant plane* in pattern space on one side of which $F = 1$ and on the other $F = 0$.

Suppose that we wish to realize the logical function of Equation (10.1) with the M–P model neuron

$$\tilde{F} = H\left(\sum_{k=1}^{3} \alpha_k V_k(t) - \theta\right), \tag{10.3}$$

where $V_1 \equiv A$, $V_2 \equiv B$, and $V_3 \equiv C$. (Recall that $H(x)$ is the Heaviside step function, which equals 0 when x is negative and 1 otherwise.)

Two questions arise: (1) How do we choose α_1, α_2, α_3, and θ? (2) If these weighting parameters are incorrectly chosen, how can they be altered so that the functions computed from Equations (10.1) and (10.3) are the same?

To answer these questions, it is convenient to define a four-dimensional *weight vector* as

$$\mathbf{W} \equiv (\alpha_1, \alpha_2, \alpha_3, -\theta)$$

and a four-dimensional *augmented pattern vector* as

$$\mathbf{P} \equiv (V_1, V_2, V_3, 1)\,.$$

Then the inner product of the weight vector and the augmented pattern vector,[1]

$$\mathbf{W} \cdot \mathbf{P} = \sum_{k=1}^{3} \alpha_k V_k(t) - \theta\,,$$

is just the argument of the Heaviside step function in Equation (10.3). Thus to realize the Boolean expression of Equation (10.1) with the M–P neuron of Equation (10.3), it suffices to choose the three α_js and θ so that the condition

$$\mathbf{W} \cdot \mathbf{P} = 0$$

corresponds to a discriminant plane lying between the vertices where $F = 1$ (the dark circles) and those where $F = 0$ (the open circles), as shown in Figure 10.1. This answers question (1).

To answer question (2), suppose that we have mistakenly chosen the components of the weight vector ($\mathbf{W_1}$) such that

$$\mathbf{W_1} \cdot \mathbf{P} < 0$$

for (say)

$$\mathbf{P} = (1, 1, 1, 1)\,,$$

but all of the other vertices in Figure 10.1 lie on the correct side of the discriminant plane. Then Equation (10.3) tells us that $\tilde{F} = 0$ for $V_1 = V_2 = V_3 = 1$. In other words, if the barometer is rising, it is daytime, and the sky is not cloudy, we should expect rain. Clearly, this is not a correct prediction and the weight vector must be changed, but how?

If the weight vector were altered by adding an increment in a direction orthogonal (at right angles) to $\mathbf{P}$, the inner product $\mathbf{W} \cdot \mathbf{P}$ would not change; thus, it is necessary to alter the weight vector in the direction of $\mathbf{P}$. To accomplish this, assume

$$\mathbf{W_2} = \mathbf{W_1} + c\mathbf{P}\,, \tag{10.4}$$

where c is a positive real constant that must be determined. Taking the inner product of both sides of Equation (10.4) with $\mathbf{P}$ and requiring that $\mathbf{W_2} \cdot \mathbf{P} > 0$ shows that for

$$c > -\frac{\mathbf{W_1} \cdot \mathbf{P}}{\mathbf{P} \cdot \mathbf{P}} \tag{10.5}$$

the inner product $\mathbf{W_2} \cdot \mathbf{P} > 0$.

[1]The inner (or "dot") product of two vectors is the sum of the products of their components.

Table 10.1. The number of Boolean networks ($\mathcal{N}$) for various numbers of switches (N).

N	$\mathcal{N} = 2^{N2^N}$
1	$2^2 = 4$
2	$4^4 = 256$
3	$8^8 \doteq 1.7 \times 10^7$
4	$16^{16} \doteq 1.8 \times 10^{19}$
5	$32^{32} \doteq 1.5 \times 10^{48}$
6	$64^{64} \doteq 3.9 \times 10^{115}$

10.2 Nets with Circles

Because the human brain is threaded through with myriad closed loops of causal implication, any serious study of its dynamics must deal with the many new entities that emerge. This section presents two constructive theories of such networks. The first indicates the degree of intricacy to be expected, and the second suggests ways in which methods of statistical physics may lead to understanding.

10.2.1 General Boolean Networks

Let us begin by imagining the most general class of networks that can be constructed from N model neurons (or switches), each of which is allowed to compute an arbitrary Boolean function of its N inputs. Because there are

$$2^{2^N}$$

Boolean functions of N inputs and each of the N neurons is chosen to be one of these, there are

$$\mathcal{N} = \left(2^{2^N}\right)^N = 2^{N2^N}$$

different systems in this class of general Boolean networks. For modest numbers of neurons, the number of possible systems soon becomes very large, as is seen from Table 10.1. To deal with such large numbers, combinatoric mathematicians have whimsically defined the *googol* $\equiv 10^{100}$ as a finite number above which arithmetic becomes problematic [11]. To see why

11
Neuronal Assemblies

Although the suggestion that neurons in the human brain may act in functional groups reaches back at least to the beginning of the twentieth century (when Charles Sherrington published his *The Integrative Action of the Nervous System* [85]), it was in Donald Hebb's classic *Organization of Behavior* that the cell-assembly concept was first carefully formulated. Largely neglected for several decades [13], Hebb's theory of neural assemblies has more recently begun to attract broad interest from the neuroscience community. Why, one wonders, was such a reasonable suggestion so long ignored? Several answers come to mind.

First, Hebb was far ahead of his time. As a psychologist, moreover, he was telling electrophysiologists and neurologists what they should be doing when these people had much on their collective plate. Throughout most of the twentieth century, electrophysiologists were facing numerous difficulties in recording from single neurons. Adequate impulse amplifiers needed to be designed and suitable microelectrodes fabricated before voltages could be measured from even a single cell. If mere hit-or-miss recordings were to be avoided, it was necessary to position accurately the tips of these electrodes, knowing what cells are located where. As the levels of the observed signals became smaller, means for shielding measurements from ambient electromagnetic noise were ever more in demand. With single-neuron recording being the primary experimental focus, therefore, it is not surprising that theoreticians refrained from embracing more complicated formulations that required simultaneous recordings from many neurons for which empirical support was not soon expected.

Second, as we have seen in Chapter 9, it is difficult enough to describe properly the dynamics of individual neurons; thus, a theory that assumed interacting assemblies of neurons would be venturing even further out onto the thin ice of speculation.

A third reason for the tendency to simplify the theoretical picture—in North America, at least—was the unfortunate domination of psychology by the beliefs of behaviorism, which focused attention on the conditioning of stimulus–response reflexes, thereby ignoring much that comprises mental reality. From the behaviorist perspective, the concept of internal cerebral states was rightly shouldered into the background because the simpler ideas of "connection theory" seemed adequate to explain acceptable psychological data.

With all of these strikes against it, how did Hebb's theory ever manage to see the light of day?

11.1 Birth of the Cell-Assembly Theory

During the 1940s, Hebb became impressed with several sorts of evidence that cast doubt on behaviorist assumptions and suggested that more subtle theoretical perspectives were needed to explain psychological facts [34]. Among such facts is the surprising robustness of the brain's dynamics, a well-known example of which was provided by railroad workman Phineas Gage, who survived having a piece of iron rod go through his brain [56]. With characteristic directness, Hebb put the matter thus: How is it that a person can register an IQ of 160 after the removal of a prefrontal lobe [32]?

His first publication on the cell assembly stemmed from observations of chimpanzees raised in a laboratory where, from birth, every stimulus was under experimental control. Such animals, Hebb noted, exhibited spontaneous fear upon seeing a clay model of a chimpanzee's head [33]. The chimps in question had never witnessed decapitation, yet some of them "screamed, defecated, fled from their outer cages to the inner rooms where they were not within sight of the clay model; those that remained within sight stood at the back of the cage, their gaze fixed on the model held in my hand" [35, 36, 38].

Such responses are clearly not reflexes; nor can they be explained as conditioned responses to stimuli, for there was no prior example in the animals' repertory of responses. Moreover, they earned no behavioral rewards by acting in such a manner. But the reactions of the chimps do make sense as disruptions of highly developed and meaningful internal configurations of neural activity according to which the chimps somehow recognized the clay head as a mutilated representation of beings like themselves.

Another contribution to the birth of his theory was Hebb's rereading of Marius von Senden's *Space and Sight* [84], which was originally published in Germany in 1932. In this work, von Senden gathered records on 65

To this end, Louie and Wilson used implanted multielectrodes to record from hippocampal CA1 pyramidal cells of rats (see Figure 9.1), which are known to be "place cells" that tend to fire when the animal is in a particular location [96]. The rats were trained to run around a circular track in search of food, and recordings were made during the actual awake activity (RUN) and also during shorter periods of "rapid eye movement sleep" (REM) [97].

Only those cells judged to be "active" (with firing rates greater than 0.2 Hz) were included in the analysis, leading to impulse train recordings from between 8 and 13 electrodes for a particular experiment. With bin sizes of 1 s and RUN recording times up to 4 minutes, the RUN-REM correlation was computed for each electrode as in Equation (11.11) and then averaged over the electrodes.

Such computations of RUN-REM correlation showed no similarity between the two measurements, but this fails to account for the possibility that the time scale of the REM signal could differ from that of awake activity (RUN). Stretching out (or slowing down) the REM data by a factor of about 2, on the other hand, gave sharply defined correlation peaks that could not be ascribed to happenstance. The authors claim that these results demonstrate that "long temporal sequences of patterned multineuronal activity suggestive of episodic memory traces are reactivated during REM sleep."

11.8 Recapitulation

This chapter opened with a survey of Donald Hebb's seminal formulation of the cell-assembly hypothesis for the robust storage and retrieval of information in the human brain and emphasized key aspects of the theory. Early evidence in support of Hebb's theory was reviewed, including the hierarchical nature of learning, perceptions of ambiguous figures, stabilized image experiments, sensory deprivation experiments, and anatomical data from the structure of the neocortex.

A simple mathematical model for interacting cell assemblies was then developed that describes ambiguous perceptions and suggests the importance of inhibitory interactions among cortical neurons for assembly formation and switching.

This model implies that cell assemblies emerge from intricate closed causal loops (subnetworks) of positive feedback threading sparsely through the neural system. Assemblies exhibit all-or-nothing response and threshold properties (just like the Hodgkin–Huxley impulse or an individual neuron); thus, an assembly is also an attractor. Interestingly, speed of switching from one assembly to another is found to increase with the level of interassembly inhibition. Under simple assumptions, a generous lower bound on the number of complex assemblies that can be stored in a human brain is estimated as about one thousand million—the number of seconds in 30 years.